Industrial Chemistry & Materials

ROYAL SOCIETY OF CHEMISTRY

PAPER

View Article Online
View Journal | View Issue

Cite this: *Ind. Chem. Mater.*, 2024, **2**, 587

Theoretical investigation of carbon dioxide adsorption on MgH_2 with a cobalt catalyst†

Sara Rozas, [a] Fabiana C. Gennari, [b] Mert Atilhan, [c] Alfredo Bol[de] and Santiago Aparicio *[ae]

This work presents a theoretical investigation of carbon dioxide (CO_2) adsorption on MgH_2 and its reaction (chemisorption) with cobalt doped MgH_2. The focus of this study is the properties and mechanisms involved in CO_2 adsorption on clean MgH_2 surfaces and the role of Co in enhancing the adsorption process. Density functional theory (DFT) calculations were performed to examine different CO_2 adsorption sites on the MgH_2 surface along with the adsorption distances, binding energies, and geometric parameters. The results indicate that physical adsorption of CO_2 occurs on MgH_2 with similar adsorption energies at different adsorption sites. The coverage effect of CO_2 molecules on MgH_2 was also investigated, revealing an increased affinity of CO_2 with higher surface coverage. However, excessive coverage led to a decrease in adsorption efficiency due to competing surface adsorption and intermolecular interactions. The orientation of adsorbed CO_2 molecules shifted from parallel to quasi-perpendicular arrangements upon adsorption, with notable deformations observed at higher coverage, which gives a hint of CO_2 activation. Furthermore, the study explores the CO_2 adsorption capacity of MgH_2 in comparison to other materials reported in the literature, showcasing its medium to strong affinity for CO_2. Additionally, the effectiveness of a single Co atom and Co clusters as catalysts for CO_2 adsorption on MgH_2 was examined. Overall, this theoretical investigation provides insights into the CO_2 adsorption properties of MgH_2 and highlights the potential of Co catalysts to enhance the efficiency of the methanation process.

Received 4th September 2023,
Accepted 21st December 2023

DOI: 10.1039/d3im00096f

rsc.li/icm

Keywords: DFT; CO_2 conversion; Cobalt catalyst; Charge transfer.

1 Introduction

Atmospheric carbon dioxide concentration reached 424.81 ppm (global mean) in June 2023,[1] which far exceeds the natural atmospheric carbon dioxide concentrations (280 ppm)[2] before the Industrial Revolution took place. This has led to severe consequences, including climate change and global warming. Carbon dioxide capture and storage, as well as carbon dioxide capture and utilisation technologies, *i.e.*, CCSs and CCUs, respectively, have been considered a suitable approach to solve this pivotal problem.[3] Among the main CO_2 capture procedures (pre-combustion, post-combustion, and oxyfuel combustion[4–6]), the post-combustion process is the most engineered technology as it can be retrofitted to existing power plants.[7] However, challenges remain, such as the requirement for high-performance materials or the demand

[a] *Department of Chemistry, University of Burgos, 09001 Burgos, Spain. E-mail: sapar@ubu.es*
[b] *National Scientific and Technical Research Council (CONICET), Bariloche Atomic Centre (CNEA), R8402AGP, S. C. de Bariloche, Río Negro, Argentina*
[c] *Department of Chemical and Paper Engineering, Western Michigan University, Kalamazoo, MI 49008-5462, USA*
[d] *Department of Physics, University of Burgos, 09001 Burgos, Spain*
[e] *International Research Center in Critical Raw Materials for Advanced Industrial Technologies (ICCRAM), University of Burgos, 09001 Burgos, Spain*

† Electronic supplementary information (ESI) available: Fig. S1 (initial dispositions of all the considered systems); Fig. S2 (optimized geometries of systems considering $n$$CO_2$ molecules); Table S1 (MgH_2 surface angle and radius deformation); Table S2 (adsorption energies for Co-catalyzed systems); Table S3 (adsorption energies for Co-catalyzed systems); Table S4 (interatomic distances between the Co atoms for the 1 to 9 cluster formation); Table S5 (interatomic distances between cobalt atoms for surface coverage); Fig. S3 (optimised geometries of Co clusters systems); Fig. S4 (optimized geometries of Co clusters systems); Fig. S5 (details of the geometric parameters of the 7Co/MgH_2 structure); Fig. S6 (optimized geometries of CO_2 on Co SAC systems); Fig. S7 (optimized geometries of CO_2 on nCo-catalyzed systems); Fig. S8 (optimized geometries of CO_2 + H_2 on Co-catalyzed systems); Table S6 (Bader ionic charges of CO_2 adsorption on clean MgH_2); Table S7 (Bader ionic charges of Co adsorption on clean MgH_2); Table S8 (Bader ionic charges of CO_2 and H_2 adsorption on Co/MgH_2); Table S9 (valence Bader charge difference for CO_2/MgH_2 systems); Table S10 (valence Bader charge difference for Co/MgH_2 systems); Table S11 (valence Bader charge difference for CO_2/Co–MgH_2 systems); Table S12 (MgH_2 surface energies for the k-point testing set); Fig. S9 (MgH_2 surface energies as a function of the selected k-points). See DOI: https://doi.org/10.1039/d3im00096f

for energy for the high sorbent regeneration process.[8] In this process, once CO_2 gas is captured by the sorption material from industrial flue gases, it can be stored in suitable geological formations[9] in the case of CCS or reused in different industrial processes in the case of CCUs. This may create extra operational needs (CCUs with conversion), such as fuels or polymeric materials,[10] or be ready to use (CCUs without conversion), such as heat transfer fluid.[11]

A possible route for CCU is methane production (methanation) from captured CO_2 through hydrogenation. CO_2 methanation is one of the most relevant applications for recycling carbon dioxide, owing to its high gravimetric heat (55.5 MJ kg^{-1}).[12] Different means for CO_2 methanation have been proposed, including photocatalytic,[13] thermal catalytic,[14] or metal-catalyzed processes,[15] among others. Recent techno-economical analyses of the most mature technologies showed several drawbacks, with the main need being the development of more efficient sorbent/catalysts to allow scaling up to the industrial level.[16] A possible route for CO_2 methanation stands on the Sabatier reaction,[17] *i.e.*, the hydrogenation reaction of CO_2 to CH_4, which is thermodynamically favourable $\left(\Delta H^{\circ}_{298} = -165\ \text{kJ mol}^{-1}\right)$[18] but must be catalyzed due to strong kinetics limitations. Likewise, the hydrogen required for the methanation may be provided to the chemical reactor[19] or it could be produced *in situ*. This last option could allows capturing and converting CO_2 simultaneously as well as ensuring the green origin of the hydrogen used.

Among the materials which can potentially be used as hydrogen sources, MgH_2 has shown a large hydrogen storage capacity.[20–22] Nevertheless, high hydrogenation/dehydrogenation temperatures remain technologically and economically unaffordable for large-scale application of MgH_2. However, Ni- and Co-additives have been shown to positively alter hydrogen absorption/desorption kinetics.[23,24] Cui *et al.*[25] confirmed that transition metal nanoparticles (NPs) of Ti, Nb, V, Co, Mo, and Ni enhance dehydrogenation performance due to a decrease in electronegativity. Dehydrogenation co-catalyzed with MgH_2 was reported by Gennari *et al.* showing hydrogen absorption/desorption temperatures dropping from 350 to 250 °C (ref. 26) and activation energies from 143 to 110 kJ mol^{-1}. Liu *et al.* reported improved hydrogen absorption/desorption performance in terms of H_2 temperature release (198.9 °C) and activation energies (76.66 kJ mol^{-1}) using Co/Pd@CNTs catalyst.[27] Therefore, taking advantage of MgH_2 material as a hydrogen source, CO_2 hydrogenation and conversion into valuable products has been assessed from an experimental point of view using MgH_2 as substrate.[28] Therefore, MgH_2 has been considered a substrate for H_2 supply in the CO_2 methanation process due to its natural capacity to release H_2 above 350 °C.[18] Theoretical studies have already been performed in this context; Manggada *et al.* employed an MgH_2 substrate for the CO_2 hydrogenation using a Mo-phosphonic acid catalyst to report a great reduction in the interaction energy barriers in the presence of the catalyst.[29] Cu/ZrO_2 system has also been evaluated in hydrogenation of CO_2 to methanol showing potential active reaction sites.[30] Moreover, Chen *et al.* reported DFT calculations revealing an enhanced weakening of the H–Mg surface bonds by introducing Mg

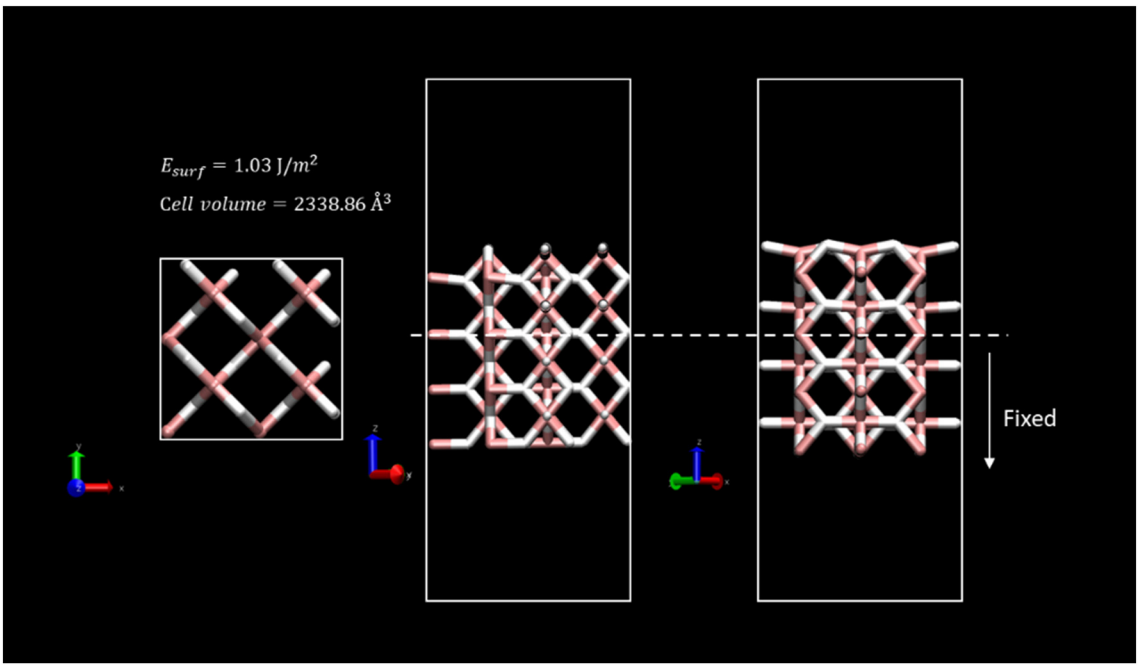

Fig. 1 Top- and two-side-view representations of the system used in the simulations. The (0 0 1) surface energy and total volume of the optimized slab after calculation are depicted. Atom colour code: (white) hydrogen, (pink) magnesium.

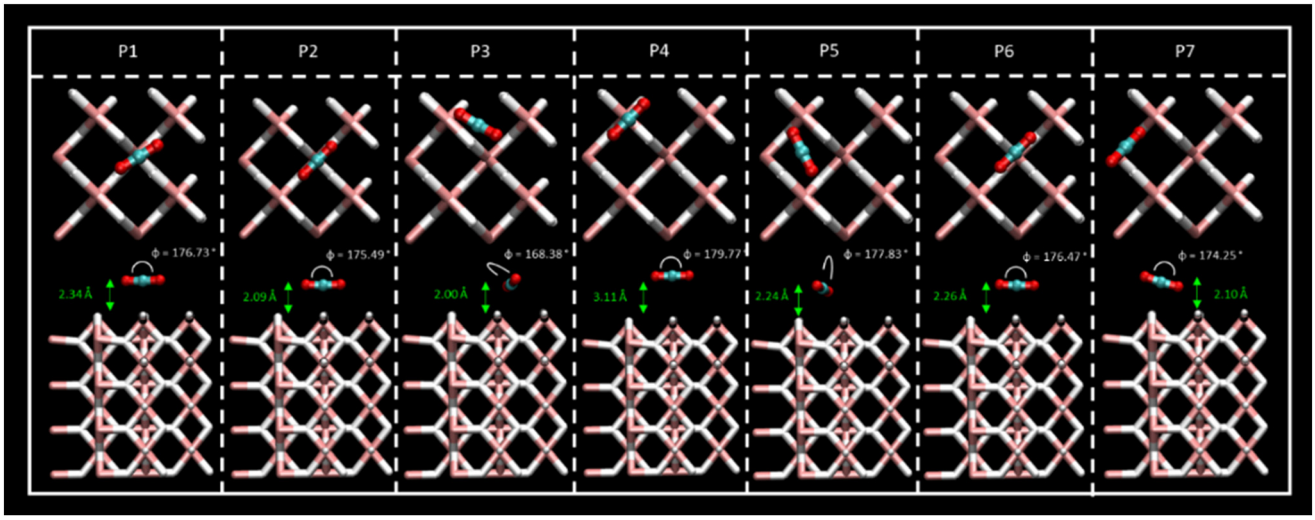

Fig. 2 Top- and side-view of the CO_2 adsorption structures for the P1–P7 sites, where CO_2 bending angles and CO_2–slab distances are shown. Atom colour code: (white) hydrogen, (pink) magnesium, (red) oxygen, (blue) carbon.

vacancies, thus facilitating CO_2 molecule adsorption on the MgH_2 substrate.[31] Experimentally, Co-based catalysts for this reaction have been studied widely.[32,33] Computational studies based on theoretical models are in demand to accurately assess and evaluate active sites in materials.[34]

CO_2 methanation assays with MgH_2 substrate as a portable hydrogen medium under thermal conditions were performed in previous work on cobalt catalysts. Results showed the mechanisms for direct CO_2 reduction to CH_4 in non-catalyzed systems, however, global mechanisms of catalyzed conversion are based on the Sabatier process that is enhanced by a Co catalyst.[35] In this regard, the aim of the present work is to analyze for the first time CO_2–MgH_2 interactions and adsorption mechanisms with and without adsorbed atoms of Co. We shed light on the driving forces and electronic properties in this reaction using a theoretical approach based on the density functional theory (DFT).

2 Results and discussion

2.1 CO_2 adsorption on clean MgH_2

Different sites for CO_2 molecule adsorption were considered on a clean MgH_2 (0 0 1) surface (Fig. 1) in accordance with the position of the molecule along with different orientations. Gas molecules were placed on top of Mg atoms, on top of H atoms, and over the interatomic cavities. In this third configuration, CO_2 molecules were parallel to the surface (*XY* plane) with two different orientations with the aim of studying all possible interactions (Fig. S1a, ESI†). Therefore, we have considered a slab model of 8.88 × 8.88 Å; seven different DFT calculations corresponding to seven initial structures for the adsorption of a single CO_2 molecule were performed. Optimised geometries for all the considered systems are shown in Fig. 2, where CO_2 bending angles and CO_2–surface distances are also reported, while binding energies and further geometric parameters are presented in Table 1. Binding energies for all the considered systems are rather similar, ranging from −0.38 to −0.43 eV, except for the P4 structure, which shows the weakest interaction energy (−0.20 eV) by far. These energies are directly related to the adsorption distances, where intervals of 2.01 to 2.34 Å were observed for P1, P2, P3, P5, P6, and P7 structures and 3.11 Å for the weak P4 adsorption site. This effect may be influenced by the electronegativity difference between O–H and O–Mg atoms. The O–H electronegativity difference is smaller than that between O–Mg, leading to weaker E_{ads}. For all the cases, CO_2 intramolecular bond lengths are maintained as before the adsorption (Fig. S1c, ESI†) except for minor alterations (±0.02 Å) in P2 and P7 structures. The angle, $\varphi_{O1–C–O2}$, shows negligible bending. The bending molecule with the largest

Table 1 Adsorption energies and geometric parameters for CO_2 adsorption on different surface sites (P1–P7) on MgH_2. The values for the configurations with the highest energy (P2 and P7) are reported in bold

	E_{ads} (eV)	$r_{C–O1}$ (Å)	$r_{C–O2}$ (Å)	φ_{CO_2} (deg)	$r_{CO_2\text{-slab}}$ (Å)
P1	−0.38	1.17	1.17	176.73	2.34
P2	**−0.41**	**1.17**	**1.17**	**175.49**	**2.09**
P3	−0.38	1.17	1.19	168.38	2.01
P4	−0.20	1.17	1.17	179.77	3.11
P5	−0.39	1.17	1.17	177.83	2.24
P6	−0.40	1.17	1.17	176.46	2.26
P7	**−0.43**	**1.16**	**1.17**	**174.25**	**2.10**

deviation from the CO_2 linear isolated molecule (179.97°, Fig. S1c, ESI†) is found in the P3 structure (168.38°). After DFT geometric optimisation, the CO_2 molecule on sites P1 and P6 underwent a reorientation, and it moved to the P2 adsorption site and showed adsorption energies (−0.38 and −0.40, respectively), molecule–surface distance (2.34 and 2.26 Å, respectively), and geometrical parameters similar to the P2 structure (E_{ads} = −0.41 eV and $r_{CO_2\text{-slab}}$ = 2.09 Å). In this adsorption position, the C atom of the CO_2 is located in a small cavity located on top of a Mg atom on the second layer on the surface, and in the middle of two H atoms on the surface. The two O atoms of the CO_2 molecule point to the Mg surface atoms perpendicular to the H atoms. The final geometry of CO_2 at P7 is also equivalent to the P2 adsorption site, but in this case, the CO_2 molecule is not fully parallel to the surface, and the binding energy is slightly larger (−0.43 eV). Therefore, P2, P3, and P5 were found to be the most active sites for CO_2 adsorption. Furthermore, CO_2 molecules starting at P3 and P5 evolve to a final position, where the C atoms are placed between two H atoms on the surface and the O atoms point again toward two Mg atoms on the surface; this CO_2 is, however, placed over the interatomic cavity (in contrast to P1, P2, P6, and P7 structures). For the latter, binding energies, CO_2–surface distances, and CO_2 geometric parameters are similar to those reported in previous systems, where the shortest CO_2–surface distance was found for the P3 structure (*i.e.*, 2.00 Å). Based on the binding energy strengths, the adsorption distances, and negligible changes in CO_2 geometry, physical adsorption of the CO_2 molecule on the MgH_2 surface can be inferred for all the proposed adsorption sites. Results agree with those reported by Chen *et al.* who explained the viability of CO_2 hydrogenation through ionic lattice hydrogen atoms.[31]

To better understand the adsorption mechanism for CO_2 gas, the effect of coverage of different CO_2 molecules was considered. The full coverage limit (1 ML) was defined as 4 CO_2 molecules (12 atoms) on top of 12 slab surface atoms (8 hydrogen + 4 magnesium atoms). Hence, an increasing number of CO_2 molecules corresponding to 0.25 ML, 0.5 ML, 0.75 ML, 1 ML, and saturated 1.25 ML were added to the MgH_2 surface (1, 2, 3, 4, and 5 molecules, respectively) according to Fig. S1b, ESI.† Surface saturation was used to evaluate the eventual reorientation of the CO_2 molecules on the MgH_2 surface. Optimized structures are shown in Fig. S2, ESI,† and the adsorption energies (per CO_2 molecule) and geometric properties of each of the adsorbed CO_2 are reported in Table 2. An increasing affinity of CO_2 molecules to the MgH_2 surface is inferred whenever enlarging surface coverage as E_{ads} scale from −0.3 to −0.4 eV (2 to 4 adsorbed molecules). This means that each molecule adsorbs more easily with an increase in coverage. Moreover, E_{ads} values agree with the ones reported for a single CO_2 molecule (P1, P2, P3, P5, P6, and P7), leading to efficient adsorption mechanisms upon coverage. However, this behaviour is not reproduced by CO_2 exceeding coverage structure (1.25 ML), where the E_{ads} drops to −0.25 eV (per CO_2 molecule). The lowering of the adsorption efficiency might be caused by the competing effects of the surface adsorption and the CO_2 intermolecular interactions imposed by the structural design constraints together with the non-availability of the most suitable surface adsorption sites (P1–P3 and P5–P7), and the surplus molecules interact at a less energetically favoured site (P4). Regarding the orientation of the adsorbed molecules, despite the initial position of the CO_2 being parallel to the surface, molecules tend to reorient after geometric optimisation toward quasi-perpendicular arrangements. This is more notable with the coverage effect. In contrast to adsorption structures with single CO_2 molecules, CO_2

Table 2 Adsorption energy (per molecule) and geometric parameters for the adsorption of *n* CO_2 molecules (*n* = 2 to 5) on MgH_2. The values for the configuration with the highest energy (4 × CO_2) are reported in bold

	n CO_2	E_{ads} (eV)	r_{C-O1} (Å)	r_{C-O2} (Å)	φ_{CO_2} (deg)	r_{CO_2-H} (Å)
2 × CO_2	1	−0.30	1.21	1.19	155.75	1.97
	2		1.16	1.17	179.18	
3 × CO_2	1	−0.36	1.28	1.23	131.50	1.18
	2		1.16	1.17	177.39	
	3		1.19	1.16	177.54	
4 × CO_2	**1**	**−0.40**	**1.26**	**1.23**	**130.91**	**1.17**
	2		**1.16**	**1.18**	**174.02**	
	3		**1.18**	**1.17**	**171.8**	
	4		**1.16**	**1.17**	**178.15**	
5 × CO_2	1	−0.25	1.28	1.25	123.94	1.06
	2		1.17	1.18	174.76	
	3		1.20	1.17	175.40	
	4		1.18	1.17	173.54	
	5		1.17	1.17	173.20	

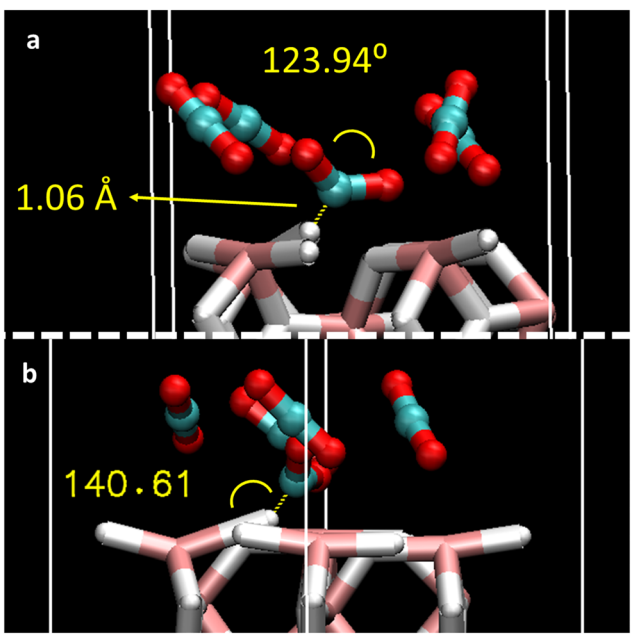

Fig. 3 Details of the geometric parameters of (a) adsorbed CO_2 bending angle and C–H4 distance and (b) Mg2–H4–C contact angle related to the CO_2 (*n* = 1) molecule behaviour in the structure of 5 adsorbed CO_2 molecules.

bending angles and bond distances for all the structures vary upon adsorption (Table 2) and with CO_2 addition. CO_2 (1) molecules located on the strongest adsorption site, *i.e.*, P2, especially deform when coverage is increased, reaching a bending angle of 123.94°, bond distances of 1.28 Å, 1.24 Å, and 1.06 Å distance to the MgH_2 surface hydrogens, when n = 5 in the coverage (Fig. 3a). At this adsorption site, slab deformation is also noticeable, especially in the ω_2 angle, which changes from 157.78° in the clean slab to 149.94° after the interaction (Table S1, ESI†). Indeed, it can be inferred that a weak H-bond might be present between H_4 (MgH_2 surface) and the C atom of CO_2 (1) because of the bond distance (1.06 Å) and interacting angle (140.61°), although electronic charge transfer could also give rise to an adsorption mechanism that also explains chemical adsorption (Fig. 3b). A comparable situation is observed at the opposite side: MgH_2 H5 atom with a C–H length of 2.41 Å and contact angle of 134.34°; a slab deformation of ω_3 changing from 157.78° to 174.35° was observed in this case (Table S1, ESI†). Alternate orientation of CO_2 molecules forming spatially perpendicular entities (non-parallel arrangement) were observed. This conformation may be adopted to avoid CO_2 quadrupole–quadrupole interactions, benefiting CO_2-slab interactions.[36] The reported effect, *i.e.*, a stronger E_{ads} when coverage with n CO_2 molecules increases, has already been described in previous literature for the CO_2 adsorption on rutile TiO_2 (1 1 0) sorbent.[37] This phenomenon will be further analysed in an upcoming section using the charge transfer phenomenon.

In summary, although the P7 position is the most stable adsorption site, adsorption energies ranging from −0.38 to −0.43 eV (except for the P4 position) indicate that the MgH_2 causes suitable physical adsorption of CO_2 molecules. The coverage effect enhances CO_2–MgH_2 surface interactions until full coverage is achieved. CO_2 molecular structure distortion and slab deformation upon CO_2 adsorption unveil possible chemical interaction between the CO_2 gas molecules and the MgH_2 sorbent. Hence, activation of the CO_2 molecule is demonstrated by the bending angle and bond distances of molecules and the CO_2–MgH_2 slab adsorption distances.

The CO_2 adsorption capacity of MgH_2 has been compared with that of diverse sorbent materials in the literature (Table 3). Clean MgH_2 slab surface shows medium to strong affinity for CO_2 molecules, and therefore, noteworthy CO_2 adsorption capacity. However, the adsorption capacities of MgH_2 are far from those provided by other kinds of materials, such as decorated metal–organic frameworks[38] (MOFs), doped monolayers,[39] γ-Al_2O_3 (1 0 0),[40] or CuO_2 (110),[41] as depicted in Table 3. Binding energies for the adsorption of a single CO_2 molecule on different materials reported in the literature, along with the DFT functional employed here, are given in Table 3.

Table 3 Adsorption energies and computational methodology of the adsorption of one CO_2 molecule on the non-catalyzed surface of different materials found in the literature

Methodology	Material	E_{ads} (eV)	Ref.
DFT-D3, PBE	**MgH_2**	**−0.41**	**This work**
DFT, PBE	MgH_2	−0.09	20
DFT-D3, PBE	Calcite (1 0 4)	−0.38	42
DFT, B3LYP	AlN monolayer	−0.15	43
DFT, PBE	TiO_2 Brookite (2 1 0)	−0.16	44
DFT, PBE	TiO_2 Anatase (1 0 1)	−0.20	45
DFT, PBE	γ-Al_2O_3 (1 1 0)	−0.43	46
DFT, PBE	γ-Al_2O_3 (1 0 0)	−0.80	32
DFT-D2, PBE	Ni (1 1 0)	−0.29	47
DFT-TS, PBE	TiO_2 anatase (1 0 1)	−0.42	48
DFT, PBE	CeO_2 (1 1 0)	−0.24	49
DFT, PBE	CuO_2 (1 1 0)	−1.22	50
DFT-vdW-DF2, PBE	V-MOF-74s	−0.55	30
DFT-D, PBE	MoS_2@GeSe monolayer	−0.96	31
DFT-D, PBE	TiO_2 rutile (1 1 0)	−0.09	29
DFT-D, PBE	BC_3 monolayer	−0.11	51
DFT-D, PBE	Cu-MOF	−0.82	52

2.2 Co-doped MgH_2

To improve CO_2 affinity to MgH_2 sorbent, the Co single-atom catalyst (SAC) and Co cluster have been proposed as catalysts for CO_2 adsorption.[33] Adsorption energies for the different interacting sites of SAC (Fig. S1, ESI†) and Co–surface distances are reported in Table 4. For the 5 possible adsorption sites considered along the MgH_2 surface, C1 and C2 structures showed larger E_{ads} values (−6.47 and −7.93 eV, respectively) than C3, C4, and C5 (−3.55 to −4.49 eV) (Table 4). Regarding geometry, the initial Co SAC position on C1 converged to the C2 position of Co as inferred through geometric parameters reported in Fig. 4 and Table 4. Thus, C1 and C2 sites can be considered equivalent, although the greater stability of the C2 SAC structure should be noted, which reflects the Co atom embracement by H1 and H2 atoms of the MgH_2 surface (Fig. 4). Despite the C1 Co–surface distances being very similar to those in C2 (Table 4), ω_2 and ω_3 surface angles deformation (Table S1, ESI†) from 157.78 to 132.37° and 133.91°, respectively, manifest the insertion of the Co atom in the MgH_2 surface structure. In contrast, for the C1 structure, ω_2 and ω_3 surface angles present negligible deformation (from 157.78 to 158.00° and 160.82° respectively) (Table S1, ESI†). For this reason, the C2 Co SAC structure was considered in the following section for CO_2 adsorption studies.

When considering multiple Co atom catalysts, stronger adsorption energies were observed on MgH_2 compared to

Table 4 Adsorption energy and geometric parameters for Co atoms (SAC) at different MgH_2 surface sites (C1–C5). The values for the configuration with the highest energy (C2) are reported in bold

	E_{ads} (eV)	$r_{Co–H1}$ (Å)	$r_{Co–H2}$ (Å)
C1	−6.47	1.52	1.50
C2	**−7.93**	**1.57**	**1.57**
C3	−4.49	2.34	2.17
C4	−3.55	1.56	1.56
C5	−4.49	1.56	1.56

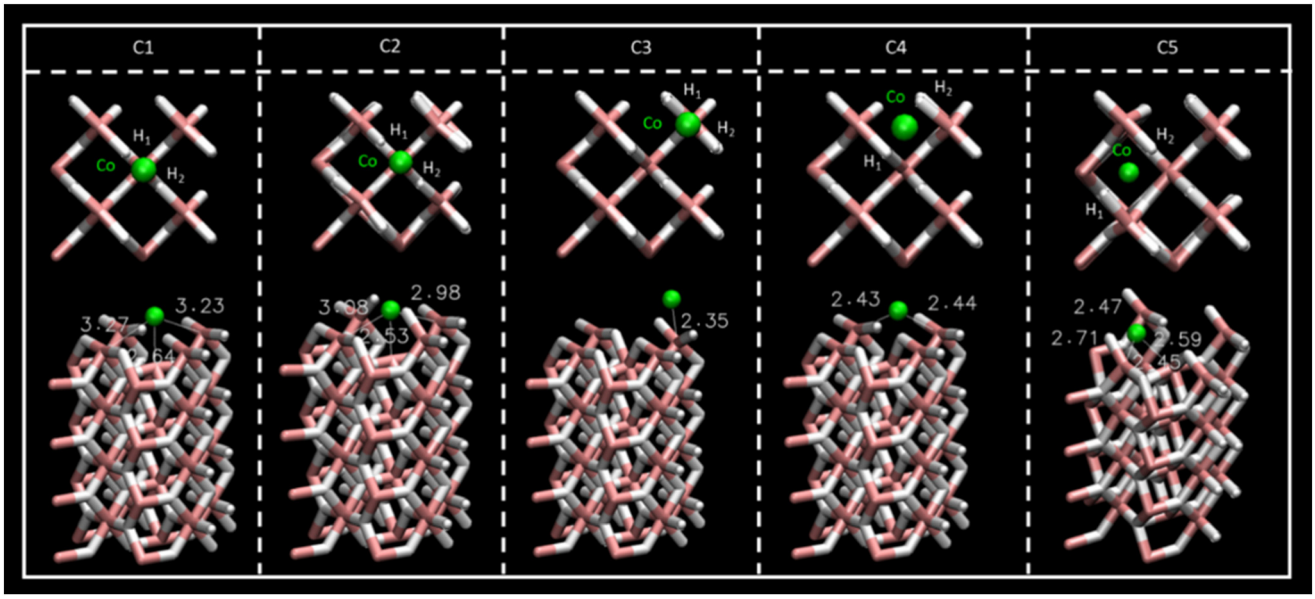

Fig. 4 Top- and side-view of the Co SAC structures for the C1–C5 sites and Co–Mg distances. Atom colour code: (white) hydrogen, (pink) magnesium, (green) cobalt.

SAC. E_{ads} (per Co atom) range from −3.09 to −10.55 eV and from −7.18 to −9.43 eV for one-by-one Co atom addition and 1/4 to full surface coverage, respectively (Tables S2 and S3, ESI†). Interatomic Co distances, which vary from 2.16 to 4.15 Å, for the one-by-one clusterization and full coverage systems (Tables S4 and S5, ESI,† respectively), agree with Co clusterization atom distances reported in the literature.[53] Catalyst adsorption on the MgH_2 surface causes geometric disruption of the first and second layers of MgH_2, and the Co embracement effect observed for the SAC structures is also reproduced for the structures with multiple Co atoms (Fig. S3 and S4, ESI†). A structure with seven Co atoms is the most energetically stable system (−10.55 eV) for *n* Co clusterization on catalyzed MgH_2. The geometric parameters (Table S1, ESI†) of the converged structure indicate that H4 and H5 atoms were displaced along the *x*-direction (Fig. S3, ESI†) and closely (1.64 and 1.62 Å) interacted with the central Co atom (Fig. S5, ESI†), while Mg2–H4 and Mg3–H5 distances extended from 1.82 Å to 2.05 and 2.51 Å, respectively (Table S1, ESI†). For the structure with full coverage of Co (4/4, Fig. S4, ESI†), the E_{ads} were slightly weaker (−9.43 eV) than that for the cluster with 7 Co atoms (Table S3, ESI†). However, the geometric disorder of the first MgH_2 layer is larger, exhibiting considerable displacement of atoms and disruption of the H–Mg–H angles (Table S1, ESI†), triggering initial structural decomposition and Co atoms integration on the MgH_2 solid surface.

For all the reported Co catalyzing structures, large adsorption energies and non-negligible changes in surface structure were found. Therefore, the Co catalyst is intended to be capable of weakening substrate bond forces, and thus, the mechanisms of interaction between CO_2 molecule and MgH_2 surface are expected to be enhanced.

2.3 CO_2 adsorption on Co/MgH_2

In this section, CO_2 and CO_2 + 2/4 H_2 adsorption on Co/MgH_2 systems are discussed. First, one CO_2 molecule adsorption on Co SAC/MgH_2 was analyzed for all the SAC structures reported in the previous section. In the case of C1

Table 5 Adsorption energy and geometric parameters for CO_2 adsorption for all the Co SAC sites on MgH_2 considered here. Both parallel (∥) and perpendicular (⊥) dispositions of the CO_2 molecule were considered. The values for the configuration with the highest energy (C3 CO_2 ∥) are reported in bold

	E_{ads} (eV)	r_{C-O1} (Å)	r_{C-O2} (Å)	φ_{CO_2} (deg)	r_{C-Co} (Å)	r_{O1-Co} (Å)
C2 CO_2 ∥	−6.61	1.20	1.20	180	1.98	
C2 CO_2 ⊥	−9.71	1.18	1.19	179.66		1.93
C3 CO_2 ∥	**−12.43**	**1.27**	**1.27**	**136.99**	**1.82**	
C3 CO_2 ⊥	−8.86	1.19	1.18	178.23		1.85
C4 CO_2 ∥	−10.17	1.23	1.29	140.19	1.81	
C4 CO_2 ⊥	−9.38	1.18	1.19	179.37		1.94
C5 CO_2 ∥	−8.42	1.28	1.24	134.94	1.98	
C5 CO_2 ⊥	−7.98	1.17	1.18	179.85		3.24

and C2 structures, only the C2 SAC position was considered as Co SAC spatial location is equivalent, and the energetic stability is stronger. Both the dispositions of the CO_2 molecule considered initially, *i.e.*, parallel and perpendicular to the surface on top of the SAC atom, manifested large CO_2 E_{ads} in the range of −6.61 to −12.43 eV (Table 5). In the case of the C2 adsorption site, CO_2 adsorption energy for the parallel disposition became smaller compared to the perpendicular disposition. However, for C3, C4, and C5 structures, parallel CO_2 disposition showed larger interacting energies with respect to the surface. In general, larger adsorption energies (more negative values) rely on stronger interactions and greater disruption of CO_2 geometric parameters (Table 5). Whereas in CO_2 perpendicular disposition, no changes were noticed in the geometry of the gas molecules, while significant structural changes were found for the parallel disposition molecule, except for CO_2 adsorption on the C2 structure. CO_2–Co SAC distances are similar for all the structures (1.81 to 1.98 Å). The C3, C4, and C5 structures featured intense disruption of the CO_2 bending angles (134.94 to 140.19°) (Table 5). Therefore, despite detecting C1 and C2 as the most stable SAC structures, CO_2 adsorption turned out to be biased for C3, C4, and C5 (in that order), as depicted through reported E_{ads} (Table 5). Adsorption on the C3 structure provides stronger interaction energy (−12.43 eV), but also the most disordered MgH_2 first layer.

Two adsorption mechanisms are inferred from this analysis: the first one and the most likely to occur (stronger interacting energy) is adsorption through the C atom of the CO_2 molecules. The second one, which is energetically weaker, is adsorption *via* the O atom with a molecular disposition perpendicular to the surface (Fig. S6, ESI†). From the former mechanism, chemical adsorption manifestation is proposed to occur based on the CO_2 and MgH_2 surface structure perturbation (Table S1, ESI†), whilst physisorption is inferred for the latter adsorption mechanism. Hence, CO_2 chemical activation through carbon atoms is observed as an effect that should be attributed to the Co catalyst.

CO_2 adsorption on a catalyst with two Co atoms on the MgH_2 surface presented much weaker adsorption energies for both parallel and perpendicular disposition of the gas molecule (−2.71 and −2.69 eV, respectively), which ended up converging in the same geometrical position (Fig. S7, ESI†). Although the distortion in the CO_2 molecular structure in the two-Co structure is slightly stronger (Table 6), the adsorption mechanisms of both the SAC and two-Co catalyst seem to behave similarly. Moderate surface deformation was observed (Table S1, ESI†).

Further investigation was carried out on the CO_2 adsorption mechanism on MgH_2 by taking into consideration H_2 molecules that mimic H_2 release from a distinct hydrogen storage substrate. Thus, 4 and 2 H_2 molecules, according to different experimentally reported methanation mechanisms (Sabatier process and direct CO_2 reduction),[26] were considered, along with one CO_2 molecule for the C2 SAC and two Co atoms catalyzing MgH_2 structures. Geometrically optimized systems displayed in Fig. S8 (ESI†) yield adsorption energies in the range of −2.61 to −3.43 eV with similar CO_2 molecule distortion geometries (Table 7). CO_2 molecule deformation is found to be in line with the previously reported adsorbed molecules, whereas H_2 molecules do not interact within the system as no structural changes occur on the molecules themselves and there are no significant interactions that could be observed within the MgH_2 surface or the CO_2 molecule either (Fig. S8, ESI†). It might be highlighted that for the C2 SAC structure interaction with 1 CO_2 and 4 H_2 molecules, the CO_2 molecule is turned parallel to the surface leading to CO_2–MgH_2 full contact, in contrast to the remaining structures (Fig. S8, ESI†). Unremarkable slab surface deformation was observed for these structures (Table S1, ESI†).

2.4 Insights into the charge transfer analysis and adsorption mechanisms

Charge density difference – or spatial charge redistribution – maps for the most stable aforementioned systems are shown in Fig. 5. Panel (a) represents the charge density for the clean slab; panels (b) to (d) depict the charge density difference of carbon dioxide on MgH_2; panels (e) to (f) show the charge density difference of Co atoms on MgH_2; and panels (h) to (k) show the charge density difference of CO_2 and H_2 on Co/MgH_2. Blue and yellow surfaces represent charge density depletion and accumulation, respectively. The difference plot slices prepared for complementary charge density in relevant

Table 6 Adsorption energy and geometric parameters for CO_2 adsorption on MgH_2 for the C2 Co SAC and the two Co atom structures. Both parallel (∥) and perpendicular (⊥) dispositions of the CO_2 molecule were considered. The values for the configuration with the highest energy (C3 CO_2 ∥ and 2 Co CO_2 ∥) are reported in bold

	E_{ads} (eV)	$r_{C–O1}$ (Å)	$r_{C–O2}$ (Å)	φ_{CO_2} (deg)	$r_{C–Co1}$ (Å)	$r_{C–Co2}$ (Å)	$r_{Co1–Co2}$ (Å)
	Co SAC/C3						
CO_2 ∥	**−12.43**	**1.27**	**1.27**	**136.99**	**1.82**		
CO_2 ⊥	−8.86	1.19	1.18	178.23		1.85	
	2 Co						
CO_2 ∥	**−2.71**	**1.24**	**1.34**	**129.37**	**1.84**	**2.24**	**2.71**
CO_2 ⊥	−2.69	1.25	1.33	130.59	1.83	2.2	2.81

Table 7 Adsorption energy (total) and geometric parameters for CO_2 and H_2 adsorption on MgH_2 for the C2 Co SAC and the two Co atom structures. System with 1 × CO_2 molecule and 2 × H_2 molecules or 1 × CO_2 molecule and 4 × H_2 molecules were considered. The values for the configuration with the highest energy (1 CO_2 + 4 H_2) are reported in bold

	E_{ads} (eV)	r_{C-O1} (Å)	r_{C-O2} (Å)	φ_{CO_2} (deg)	r_{C-Co1} (Å)	r_{C-Co2} (Å)	$r_{Co1-Co2}$ (Å)	r_{H1-H2} (Å)
	Co SAC/C2							
1 CO_2 + 2 H_2	−2.61	1.26	1.26	136.72	1.83	—	—	0.75
1 CO_2 + 4 H_2	**−3.43**	**1.32**	**1.25**	**129.73**	**1.80**	—	—	**0.75**
	2 Co							
1 CO_2 + 2 H_2	−3.10	1.28	1.28	136.36	1.90	1.90	2.66	0.75
1 CO_2 + 4 H_2	**−3.43**	**1.28**	**1.29**	**136.36**	**1.90**	**1.89**	**2.66**	**0.75**

regions of the system aid in comprehending the charge density transfer effect (Fig. 6), where red and blue colours represent maximum and minimum charge density accumulation, respectively. In panels (b) to (d) of Fig. 5, charge accumulation around oxygen and surface hydrogen atoms is outlined, whereas atomic charge depletion is observed for central carbon atoms, justifying the physisorption effect. Moderate charge transfer between CO_2 molecules and MgH_2 is shown, except for the CO_2 (2) molecules in panel (d), Fig. 5. Contrarily, large charge density transfer can be observed along with Co adsorption on the MgH_2 surface. The chemisorption of Co SAC on the MgH_2 surface is confirmed through strong charge interactions. An analogous effect is observed for the subsequent addition of Co atoms (Fig. 5f and g). More complex charge transfer patterns are observed in panels h to k. Combining panels (h) to (k) of Fig. 5 and 6, we can observe a double charge transfer effect: first, from the Co atoms adsorbed to the H atoms on the MgH_2 surface, and second, from the carbon of the CO_2 molecule adsorbed to the Co catalyst atoms. Hydrogen molecules do not seem to interchange charge density either with catalyzing surface or CO_2 molecules as no surfaces are associated with H_2 molecules.

Lastly, to gain insight into the CO_2 adsorption mechanisms, charge density transfer was investigated *via* valence Bader charges analysis. Valence electronic charges for CO_2 and H_2 molecules, first and second layers of MgH_2 and Co atoms were considered before and after the adsorption of the corresponding atoms/molecules (Tables S6–S8, ESI†). Next, charge transfer was calculated as the difference between the isolated surface/CO_2 molecule/Co atom and the valence Bader charges for the overall systems of the CO_2

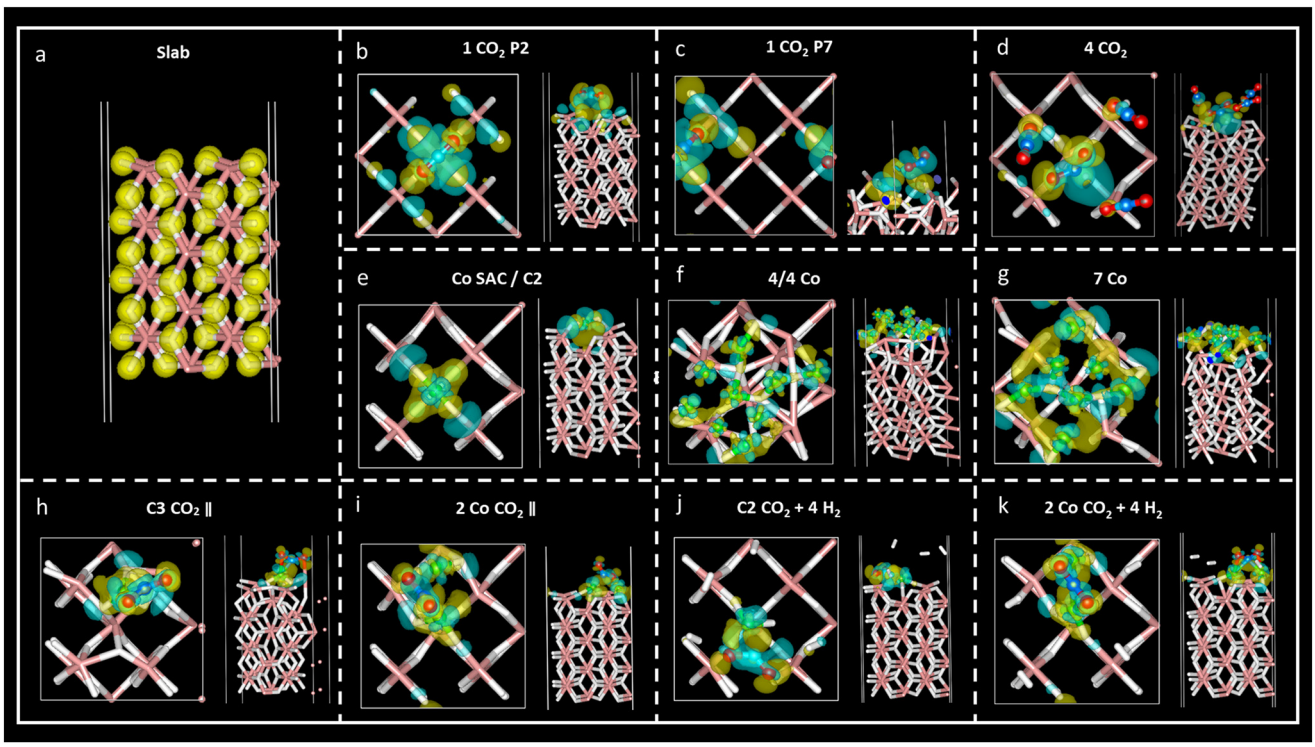

Fig. 5 Charge density difference maps ($\rho_{system} - \rho_{slab} - \rho_{Co} - \rho_{gas}$) for the most stable structures (a–k) with the isosurface value of 0.005e. The yellow region represents charge density accumulation, while the blue region represents charge depletion.

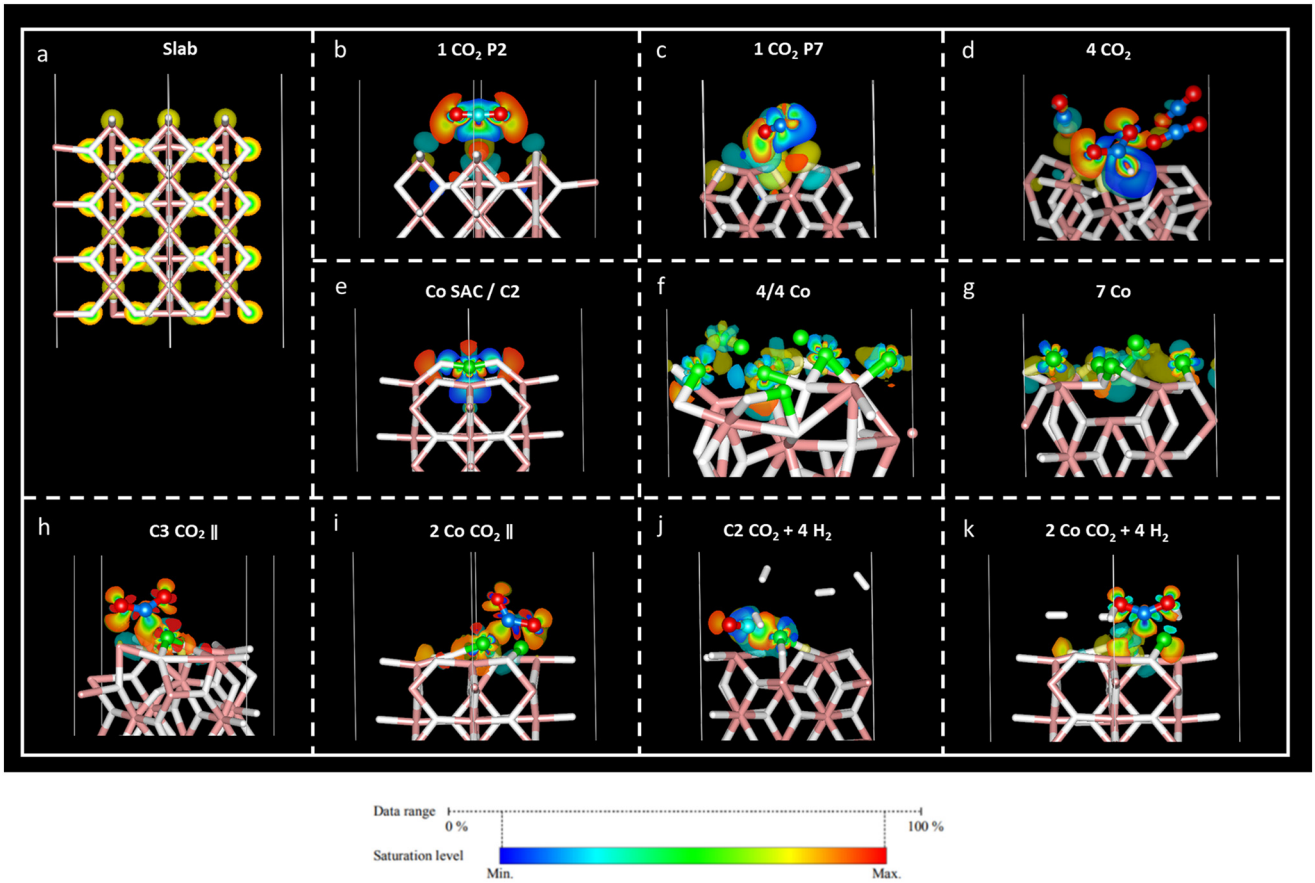

Fig. 6 Charge density difference slice for the most stable structures (a–k) considering an isosurface value of 0.005e. Red-like colours represent charge density accumulation, while the region leaning to blue shades represents charge depletion.

molecule adsorbed on a clean MgH_2 surface, Co atom adsorbed on a clean MgH_2 surface, and CO_2/H_2 adsorbed on the catalysing systems (Tables S8–S10, ESI,† respectively). Positive and negative charge differences indicate charge uptake and charge loss, respectively. This means that an atom with a positive charge difference has electronic charge accumulation (negative ionic charge). Given the reported results, minor charge differences between CO_2 atoms and MgH_2 surface atoms confirm the physisorption mechanism at P2 and P7 sites (Table S9, ESI†). However, a significant charge difference was found within the CO_2 atoms: uptake of electronic charge by O atoms (+0.76 to +0.85) from the central C atom (which losses −1.51 and −1.67, respectively), favouring weak van der Waals interactions with the hydrogens on the MgH_2 surface (Table 1).

In the case of the four-CO_2-molecules system, physical adsorption could be inferred for CO_2 (1), CO_2 (3), and CO_2 (4) molecules on MgH_2, but chemisorption was confirmed for the CO_2 (2) molecule as significant charge transfer was observed between the H_4 and C_1 (2) atoms (Table S9, ESI†). This result is validated by the previously observed bending angle of the gas molecule, as well as adsorption distance (Table 2) and accumulation/depletion charge density map (Fig. 5d).

The charge difference reported for Co atoms on MgH_2 confirms strong interactions between the sorbent and selected catalyst as a large charge transfer was found between the hydrogen atoms on the surface and Co atoms (Table S11, ESI†). Therefore, strong adsorption of Co atoms on the MgH_2 surface was also corroborated by large adsorption energies and short interatomic distances (Tables 4, S2, and S3, ESI†). The charge difference of Co_4, Co_5, and Co_9 (Co atoms on the top of the surface H atoms), as well as Co_4, for seven Co and 4/4 systems, respectively, are particularly pronounced according to charge density maps (Fig. 5f and g).

Finally, the CO_2 and H_2 adsorption on the catalysis systems depicted moderate charge transfer between the MgH_2 surface and Co atoms combined with CO_2 adsorption on top of the Co atoms. In these structures, partial charge transfer from the C central CO_2 atom developed toward the O atoms, in parallel to partial charge transfer to the Co catalyst, leading to large ionic charge accumulation on the Co atoms. Thus, strong interactive forces between the CO_2 gas molecules and the catalysis surface are confirmed. Along with large E_{ads} and short adsorption distances, these findings corroborate the chemical nature of the adsorption mechanism. Additionally, considerable charge density is distributed along the CO_2 oxygen atoms, which may lead to

possible interactive sites for H_2 adhesion. However, despite that, low reactivity was found for H_2 molecules according to the reported charge transfer and charge density plots.

Based on the reported results, two main conclusions can be reached: i) high CO_2 adsorption capacity of MgH_2 was confirmed with a preferential physisorption mechanism for the clean surface and a chemisorption route for the Co-catalysed surface, and ii) no interaction could be detected between the adsorbed CO_2 and H_2 molecules.

3 Conclusions

In this theoretical inquiry, we systematically investigated the properties and mechanisms governing carbon dioxide (CO_2) adsorption on magnesium hydride (MgH_2) surfaces augmented with Co atoms. The focal point of our analysis was an unaltered MgH_2 surface and the impact of Co species on the CO_2 adsorption process. The findings unveiled the physical manifestation of the adsorption phenomena on the MgH_2 surface, whereby disparate adsorption sites are present indicating uniform adsorption energies. The influence of CO_2 molecular coverage on MgH_2 demonstrated increased affinity at enhanced surface coverage, reaching an optimal saturation point after which excessive coverage occurred and induced a decline in adsorption efficiency. Following adsorption, the orientational configuration of CO_2 molecules transitioned from parallel to quasi-perpendicular arrangements, accompanied by discernible deformations at heightened coverage.

In the context of comparative analyses with alternative materials, MgH_2 emerged as a noteworthy medium with a strong affinity for CO_2. Furthermore, our scrutiny of the efficacy of Co single atoms or clusters for CO_2 adsorption on MgH_2 indicated the superiority of Co single atoms for adsorption at specific sites that were reflected in heightened adsorption energies. This mechanism entails the activation of CO_2 molecules through perturbation of molecular properties, characterisation of CO_2–MgH_2 slab interactions, and facilitation of electronic charge transfer.

These observations collectively contribute to a deep comprehension of the underlying properties and mechanisms of CO_2 adsorption on MgH_2 in the presence of Co. Importantly, they provide pivotal insights into the initial reaction step, thereby guiding the rational design of more efficient CO_2 conversion technologies.

4 Computational methods

Quantum Espresso 6.5 software[54] with the PW package was used for DFT spin-polarised calculations. For all the atoms involved in simulations, projector augmented wave (PAW) pseudopotentials were used,[55,56] together with the revised version[57] of the PBE exchange–correlation functional.[50,58,59] Periodic boundary conditions (PBC) were applied, and dispersion forces were also included *via* the semi-empirical correction by Grimme, DFT-D3.[60] The Burai graphical user interface of Quantum Espresso was used to build the systems. The DMol3 package from the BIOVIA materials studio environment was also employed for geometry pre-optimisation and initial systems equilibration (DFT-PBE).

Magnesium hydride is characterized by a tetragonal crystal system with a $P4_2/mnm$ space group (α-MgH_2).[61,62] Experimental lattice parameters are $a = b = 4.512$ Å and $c = 3.016$ Å.[63] From this data, bulk lattice was relaxed with a k-point Monkhorst–Pack grid[64] of 12 × 12 × 12, which was converged before considering production runs (see Table S12 and Fig. S9, ESI†) to allow the necessary energy accuracy, along with a cut-off energy of 40 Ry (544.23 eV), according to the largest value recommended in the employed pseudopotentials.

The new lattice parameters of the relaxed system were $a = b = 4.503$ Å and $c = 3.01$ Å. To mimic the bulk crystal, a 2 × 2 supercell with 4 layers of depth was generated. A surface with (0 0 1) Miller index was considered for the slab model since it is the most suitable surface regarding vacancy formation energies, and thus, the dehydrogenation process.[48,65] A twenty-Angstrom vacuum layer was set above the model slab to avoid the interaction of neighbouring MgH_2 cells. For all the calculations, two bottom layers of the slab were fixed to maintain crystal behaviour. Fig. 1 shows the overall simulated cell of dimensions, 8.88 × 8.88 × 30.47 Å, enclosing 96 atoms.

Surface energy, E_{surf}, for the clean MgH_2 slab was calculated according to eqn (1) because the symmetry of the two-sided slab guarantees the double counting of the surface energy. E_{bulk} is the energy of the bulk MgH_2, and A_{slab} is the surface area of a side of the calculated supercell slab model.

$$E_{surf} = \frac{E_{slab} - \left(\frac{N_{slab}}{N_{bulk}}\right)E_{bulk}}{2A_{slab}} \quad (1)$$

In this formula, N_{slab} is the number of atoms on the slab, and N_{bulk} is the number of atoms in the bulk material.

Once the E_{surf} of the clean MgH_2 slab and the energy E_{CO_2} of the isolated CO_2 molecule were computed, CO_2 adsorption energy (E_{ads}) on non-catalyzing systems was also calculated for different positions of the carbon dioxide molecule (P1–P7) as well as for different numbers of the CO_2 molecules (n = 1–5) according to eqn (2):

$$E_{ads} = (E_{surf+nCO_2} - E_{surf} - nE_{CO_2})/n \quad (2)$$

Co-doped systems were then examined; first, by considering one cobalt atom as the SAC, C1–C5, followed by n = 1–9 cobalt atoms in a growing plain cluster disposition; lastly, accounting for partial to full cobalt surface coverage layouts (1/4, 2/4, 3/4, and 4/4 of the slab surface). The energies of catalyzing systems were calculated as follows (eqn (3)):

$$E_{int\ Co/MgH_2} = (E_{surf+nCo} - E_{surf} - nE_{Co})/n \quad (3)$$

Accordingly, CO_2 adsorption energy (E_{ads}) on the catalyzing systems was evaluated for different dispositions of one CO_2 molecule (parallel and perpendicular arrangement with respect to the MgH_2 surface) and for one molecule of CO_2 and 2–4 hydrogen molecules (in agreement with 1 : 2 and 1 : 4 CO_2/H_2 reaction ratio) to understand interaction mechanisms. One Co SAC and two Co-catalyzed MgH_2 systems were considered in this section. eqn (4) describes CO_2 or CO_2 + 2/4 H_2 adsorption energies:

$$E_{ads} = E_{n\mathrm{Co/MgH_2}+n\mathrm{CO_2}+n\mathrm{H_2}} - E_{n\mathrm{Co/MgH_2}} - nE_{\mathrm{CO_2}} - nE_{\mathrm{H_2}} \quad (4)$$

For the systems in which more than one carbon dioxide molecule or hydrogen molecule is considered, the calculated adsorption energy was divided by the number of molecules to estimate the adsorption energy per molecule. In Fig. S1, ESI,† top view of the considered positions for one CO_2 molecule (P1–P7, Fig. S1a, ESI†) and 1 to 5 CO_2 molecules (Fig. S1b, ESI†) over MgH_2 (0 0 1) surface are shown as well as the initial bond distances and bending angle of the optimized carbon dioxide molecule (Fig. S1c, ESI†). Accordingly, SAC positions of Co (C1–C5), Co clusterization (1 Co–9 Co), and Co coverage arrangements (1/4 Co, 2/4 Co, 3/4 Co, and 4/4 Co) are shown in Fig. 1d, S1e and f, ESI,† respectively.

To elucidate the CO_2 adsorption mechanism and CO_2 + H_2 interactions over MgH_2 (0 0 1) surface catalyzed and non-catalyzed by Co, charge density differences obtained from electron (pseudo-) charge density quantum espresso plots were evaluated. The final spatial distribution of electronic charge density upon CO_2/Co/H_2 adsorption was calculated by subtracting the charge densities of the CO_2/Co/H_2 entity (ρ_{MgH_2}, ρ_{Co}, ρ_{CO_2}, ρ_{H_2}, respectively) from the entire final system, $\rho_{\mathrm{Co/MgH_2}+\mathrm{CO_2}+\mathrm{H_2}}$ according to eqn (5):

$$\rho_{final} = \rho_{sys} - \rho_{MgH_2} - \rho_{Co} - \rho_{CO_2} - \rho_{H_2} \quad (5)$$

VESTA and VMD were used to visualize charge density differences and to evaluate charge transfer results. Bader charges of the valence electrons were also evaluated for the largest energy configurations. For this purpose, the Bader code by the Henkelman group[66–69] was employed to identify single atoms inside the system and evaluate their charge density allowing the evaluation of charge transfer phenomena upon adsorption.

Data availability statement

The data that support the findings of this study are available from the corresponding author upon reasonable request.

Conflicts of interest

The authors declare no conflict of interest.

Acknowledgements

This investigation was funded by the CO_2 absorbing Materials Project-RISE (CO2MPRISE) which received funding from the European Union's Horizon 2020 research and innovation program under the Marie Skłodowska-Curie Grant Agreement No. H2020-MSCA-RISE-2016-CO2MPRISE-734873. We also acknowledge SCAYLE (Supercomputación Castilla y León, Spain) for providing supercomputing facilities. The statements made herein are solely the responsibility of the authors.

References

1 Global Monitoring Laboratory, Earth System Research Laboratories, **https://gml.noaa.gov/ccgg/trends/**, (accessed July 2023).
2 IPCC, *Climate Change 2007. The Physical Science Basis*, Cambridge Univ. Press, Cambridge, 2007.
3 F. Kazemifar, A review of technologies for carbon capture, sequestration, and utilization: Cost, capacity, and technology readiness, *Greenhouse Gases: Sci. Technol.*, 2022, **12**, 200–230.
4 P. Markewitz, W. Kuckshinrichs, W. Leitner, J. Linssen, P. Zapp, R. Bongartz, A. Schreiber and T. E. Müller, Worldwide innovations in the development of carbon capture technologies and the utilization of CO2, *Energy Environ. Sci.*, 2012, **5**, 7281–7305.
5 N. S. Sifat and Y. Haseli, A critical review of CO2 capture technologies and prospects for clean power generation, *Energies*, 2019, **12**, 4143.
6 A. Sood, A. Thakur and S. M. Ahuja, Recent advancements in ionic liquids-based carbon capture technologies, *Chem. Eng. Commun.*, 2021, **210**, 933–954.
7 B. Dutcher, M. Fan and A. G. Russell, Amine-based CO2 capture technology development from the beginning of 2013 – A review, *ACS Appl. Mater. Interfaces*, 2015, **7**, 2137–2148.
8 A. I. Osman, M. Hefny, M. I. A. Abdel Maksoud, A. M. Elgarahy and D. W. Rooney, Recent advances in carbon capture storage and utilization technologies: A review, *Environ. Chem. Lett.*, 2021, **19**, 797–849.
9 A. Raza, R. Gholami, R. Rezaee, V. Rasouli and M. Rabiei, Significant aspects of carbon capture and storage–A review, *Petroleum*, 2019, **5**, 335–340.
10 K. M. K. Yu, I. Curcic, J. Gabriel and S. E. Tsang, Recent advances in CO2 capture and utilization, *ChemSusChem*, 2008, **1**, 893–899.
11 G. Cau, D. Cocco and V. Tola, Performance and cost assessment of Integrated Solar Combined Cycle Systems (ISCCSs) using CO2 as heat transfer fluid, *Sol. Energy*, 2012, **86**, 2985–2985.
12 R. C. Weast, *CRC handbook of chemistry and physics*, CRC Press, Boca Raton, 1973–1974.
13 U. Ulmer, T. Dingle, P. N. Duchesne, R. H. Morris, A. Tavasoli, T. Wood and G. A. Ozin, Fundamentals and applications of photocatalytic CO2 methanation, *Nat. Commun.*, 2019, **10**, 3169.

14 Z. Liu, X. Gao, B. Liu, Q. Ma, T. S. Zhao and J. Zhang, Recent advances in thermal catalytic CO2 methanation on hydrotalcite-derived catalysts, *Fuel*, 2022, **321**, 12411.
15 J. Ashok, S. Pati, P. Hongmanoram, Z. Tianxi and C. Junmei, A review of recent catalyst advances in CO2 methanation processes, *Catal. Today*, 2020, **356**, 471–489.
16 Z. Lv, H. Du, S. Xu, T. Deng, J. Ruan and C. Qin, Techno-economic analysis on CO2 mitigation by integrated carbon capture and methanation, *Appl. Energy*, 2024, **355**, 122242.
17 A. Tripodi, F. Conte and I. Rosetti, Carbon Dioxide Methanation: Design of a Fully Integrated Plant, *Energy Fuels*, 2020, **34**, 7242–7256.
18 P. Sabatier and J. B. Senderns, Mouvelles synthese du methane, *C. R. Acad. Sci.*, 1902, **134**, 514–516.
19 K. Fakumoto, W. Zhang, R. Mizoguchi, Y. Lin, C. Chai, H. Machida and K. Narinaga, CFD simulation of CO2 methanation through the Sabatier reaction in a shell-and-tube reactor incorporating phase change on the shell side, *Fuel*, 2023, **349**, 128126.
20 Q. Hou, X. Yang and J. Zhang, Review on Hydrogen Storage Performance of MgH2: Development and Trends, *ChemistrySelect*, 2021, **6**, 1589–1606.
21 E. M. Dematteis, J. Barale, M. Corno, A. Sciullo, M. Baricco and P. Rizzi, Solid-state hydrogen storage systems and the relevance of a gender perspective, *Energies*, 2021, **14**, 6158.
22 C. N. C. Hitman, M. A. A. Aziz, A. H. Ruhaimi and M. R. Taib, Magnesium-based alloys for solid-state hydrogen storage applications: A review, *Int. J. Hydrogen Energy*, 2021, **46**, 31067–31083.
23 O. Zavorotynska, I. Saldan, S. Hino, T. D. Humphries, S. Deledda and B. C. Hauback, Hydrogen cycling in γ–Mg(BH4)2 with cobalt-based additives, *J. Mater. Chem. A*, 2015, **3**, 6592–6602.
24 I. Saldan, S. Hino, T. D. Humphries, O. Zavorotynska, M. Chong, C. M. Jensen, S. Deledda and B. C. Hauback, Structural changes observed during the reversible hydrogenation of Mg(BH4)2 with Ni-based additives, *J. Phys. Chem. C*, 2014, **118**, 23376–23384.
25 J. Cui, J. Liu, H. Wang, L. Ouyang, D. Sun, M. Zhu and X. Yao, Mg-TM (TM: Ti, Nb, V, Co, Mo or Ni) core-shell like nanostructures: Synthesis, hydrogen storage performance and catalytic mechanism, *J. Mater. Chem. A*, 2014, **2**, 9645–9655.
26 M. G. Verón, H. Troiani and F. C. Gennari, Synergetic effect of Co and carbon nanotubes on MgH2 sorption properties, *Carbon*, 2011, **49**, 2413–2423.
27 M. Liu, X. Xiao, S. Zhao, M. Chen, J. Mao, B. Luo and L. Chen, Facile synthesis of Co/Pd supported by few-walled carbon nanotubes as an efficient bidirectional catalyst for improving the low temeprature hydrogen storage properties of magnesium hydride, *J. Mater. Chem. A*, 2019, **7**, 5277–5287.
28 M. L. Grasso, L. Fernández Albanesi, S. Garroni, G. Mulas and F. C. Gennari, Methane production by mechanochemical processing of MgH2-Li2CO3 as sources of H2 and CO2 at room temperature, *J. CO2 Util.*, 2020, **40**, 101209.
29 G. W. Manggada and S. Zhou, Phosphonic acid modification to molybdenum atom catalyst for CO2 hydrogenation on magnesium hydride surface, *DISTILAT: Jurnal Teknologi Separasi*, 2022, **8**, 315–324.
30 S. Polierer, J. Jelic, S. Pitter and F. Studt, On the reactivity of the Cu/ZrO2 system for the hydrogenation of CO2 to methanol: A density functional theory study, *J. Phys. Chem. C*, 2019, **123**, 26904–26911.
31 H. Chen, P. Liu, J. Li, Y. Wang, C. She, J. Liu, L. Zhang, Q. Yang, S. Zhou and X. Feng, MgH2/CuxO hydrogen storage composite with defect-rich surfaces for carbon dioxide hydrogenation, *ACS Appl. Mater. Interfaces*, 2019, **11**, 31009–31017.
32 V. Iablokow, S. K. Beaumnt, S. Alayoglu, V. V. Pushkarev, C. Specht, J. Gao, A. P. Alivisatos, N. Kruse and G. A. Somorjai, Size-controlled model Co nanoparticle catalyst for CO2 hydrogenation: Synthesis, characterization, and catalytic reactions, *Nano Lett.*, 2012, **12**, 3091–3096.
33 G. Zhou, T. Wu, H. Xie and X. Zheng, Effect of structure on the carbon dioxide methanation performance of Co-based catalyst, *Int. J. Hydrogen Energy*, 2013, **38**, 10012–10018.
34 A. Morales-García, F. Viñes, J. R. B. Gomes and F. Illas, Concepts, models, and methods in computational heterogeneous catalysis illustrated through CO2 conversion, *Wiley Interdiscip. Rev.: Comput. Mol. Sci.*, 2021, **11**(4), e1530.
35 M. L. Grasso, S. Rozas, P. A. Larochette, S. Aparicio and F. Gennari, Thermochemical transformation of CO2 for CH4 production using metal hydride and carbonates as portable sources, *Int. J. Hydrogen Energy*, 2023, **48**, 21835–24849.
36 A. J. Stone, *The theory of intermolecular forces*, Oxford University Press, New York, 1997.
37 C. Sorescu, J. Lee, W. A. Al-Saidi and K. D. Jordan, CO2 adsorption on TiO2(110) rutile: Insight from dispersion-corrected density functional theory calculations and scanning tunneling microscopy experiments, *J. Chem. Phys.*, 2011, **134**, 104707.
38 K. Lee, J. D. Howe, L.-C. Lin, B. Smith and J. B. Neaton, Small-molecule adsorption in open-site metal–organic frameworks: A systematic density functional theory study for rational design, *Chem. Mater.*, 2015, **27**, 668–678.
39 H. Yang, C. He, L. Fu, J. Huo, C. Zhao, X. Li and Y. Song, Capture and separation of CO2 on BC3 nanosheets: A DFT study, *Chin. Chem. Lett.*, 2021, **32**, 3202–3206.
40 Y. Pan, C.-J. Liu and Q. Ge, Adsorption and protonation of CO2 on partially hydroxylated γ-Al2O3 surfaces: A density functional theory study, *Langmuir*, 2008, **24**, 12410–12419.
41 A. K. Mishra, A. Roldan and N. H. Leeuw, A density functional theory study of the adsorption behavior of CO2 on CuO2 surfaces, *J. Chem. Phys.*, 2016, **145**, 4958804.
42 G. Carchini, I. Hussein, M. J. Al-Marri, R. Shawabkeh, M. Mahamoud and S. Aparicio, A theoretical study of gas adsorption on calcite for CO2 enhanced natural gas recovery, *Appl. Surf. Sci.*, 2020, **504**, 144575.
43 Y. Jiao, A. Du, Z. Zhu, V. Rudolph and S. C. Smith, Adsorption of carbon dioxide and nitrogen on single-layer aluminum nitride nanostructures studied by

density functional theory, *J. Phys. Chem. C*, 2010, **114**, 7846–7849.
44 M. M. Rodriguez, X. Peng, L. Liu, Y. Li and J. M. Andino, A density functional theory and experimental study of CO2 interaction with brookite TiO2, *J. Phys. Chem. C*, 2012, **116**, 19755–19764.
45 D. C. Sorescu, W. A. Al-Saidi and K. D. Jordan, CO2 adsorption on TiO2 (1 0 1) anatase: A dispersion-corrected density functional theory study, *J. Chem. Phys.*, 2011, **135**, 124701.
46 Y. Pan, C.-J. Liu and Q. Ge, Adsorption and protonation of CO2 on partially hydroxylated γ-Al2O3 surfaces: A density functional theory study, *Langmuir*, 2008, **24**, 12410–12419.
47 O. Mohan, Q. T. Trinh, A. Benerjee and S. H. Mushrif, Predicting CO2 adsorption and reactivity on transition metals surfaces using popular density functional theory methods, *J. Exp. Nanosci.*, 2019, **45**, 1163–1172.
48 V. Chihaia, D. A. Neacsu, V. Alexiev and D. Angelescu, Performances of the bond order interacting potentials on calculating the surface energies of MgH2 facets, Available at SSRN: **https://ssrn.com/abstract=4282784**.
49 N. Kumari, N. Sinha, M. A. Haider and S. Basu, CO2 reduction to methanol on CeO2 (1 1 0) surface: A density functional theory study, *Electrochim. Acta*, 2015, **170**, 21–29.
50 J. P. Perdew, K. Bruke and M. Ernzerhof, Generalized gradient approximation made simple, *Phys. Rev. Lett.*, 1996, **77**, 3865–3868.
51 H. Yang, C. He, L. Fu, J. Huo, C. Zhao, X. Li and Y. Song, Capture and separation of CO2 on BC3 nanosheets: A DFT study, *Chin. Chem. Lett.*, 2021, **32**, 3202–3206.
52 Q. Cui, G. Qin, W. Wang, K. R. Geethalakshmi, A. Du and Q. Sun, Novel two-dimensional MOF as promising single-atom electrocatalyst for CO2 reduction: A theoretical study, *Appl. Surf. Sci.*, 2020, **500**, 143993.
53 B. Farkas and N. H. Leeuw, Towards a morphology of cobalt nanoparticles: Size and strain effects, *Nanotechnology*, 2020, **31**, 195711.
54 P. Giannozzi, S. Baroni, N. Bonini, M. Calandra, R. Car, C. Cavazzoni, D. Ceresoli, G. L. Chiarotti, M. Cococcioni, I. Dabo, A. Dal Corso, S. de Gironcoli, S. Fabris, G. Fratesi, R. Gebauer, U. Gerstmann, C. Gougoussis, A. Kokalj, M. Lazzeri, L. Martin-Samos, N. Marzari, F. Mauri, R. Mazzarello, S. Paolini, A. Pasquarello, L. Paulatto, C. Sbraccia, S. Scandolo, G. Sclauzero, A. P. Seitsonen, A. Smogunov, P. Umari and R. M. Wentzcovitch, QUANTUM ESPRESSO: a modular and open-source software project for quantum simulations of materials, *J. Phys.: Condens. Matter*, 2009, **21**, 395502.
55 P. E. Blöchl, Generalized separable potentials for electronic-structure calculations, *Phys. Rev. B*, 1990, **41**, 5414–5416.
56 G. Kresse and D. Joubert, From ultrasoft pseudopotentials to the projector augmented-wave method, *Phys. Rev. B*, 1990, **59**, 1758–1775.
57 Y. Zhang and W. Yang, Comment on "Generalized Gradient Approximation Made Simple", *Phys. Rev. Lett.*, 1998, **80**, 890–890.
58 G. Prandini, A. Marrazzo, I. E. Castelli, N. Mounet and N. Marzari, Precision and efficiency in solid-state pseudopotential calculations, *npj Comput. Mater.*, 2018, **4**, 72.
59 K. Lejaeghere, G. Bihlmayer, T. Björkman, P. Blaha, S. Blügel, V. Blum, D. Caliste, I. E. Castelli, S. J. Clark, A. Dal Corso, S. de Gironcoli, T. Deutsch, J. K. Dewhurst, I. Di Marco, C. Draxl, M. Dułak, O. Eriksson, J. A. Flores-Livas, K. F. Garrity, L. Genovese, P. Giannozzi, M. Giantomassi, S. Goedecker, X. Gonze, O. Grånäs, E. K. U. Gross, A. Gulans, F. Gygi, D. R. Hamann, P. J. Hasnip, N. A. W. Holzwarth, D. Iuşan, D. B. Jochym, F. Jollet, D. Jones, G. Kresse, K. Koepernik, E. Küçükbenli, Y. O. Kvashnin, I. L. M. Locht, S. Lubeck, M. Marsman, N. Marzari, U. Nitzsche, L. Nordström, T. Ozaki, L. Paulatto, C. J. Pickard, W. Poelmans, M. I. J. Probert, K. Refson, M. Richter, G.-M. Rignanese, S. Saha, M. Scheffler, M. Schlipf, K. Schwarz, S. Sharma, F. Tavazza, P. Thunström, A. Tkatchenko, M. Torrent, D. Vanderbilt, M. J. van Setten, V. Van Speybroeck, J. M. Wills, J. R. Yates, G.-X. Zhang and S. Cottenier, Reproducibility in density functional theory calculations of solids, *Science*, 2016, **351**, aad3000.
60 S. Grimme, J. Antony, S. Ehrlich and H. Krieg, A consistent and accurate ab initio parametrization of density functional disersion correction (DFT-D) for the 94 elements H-Pu, *J. Chem. Phys.*, 2010, **132**, 15104.
61 J.-P. Bastide, B. Bonnetot, J.-M. Létoffé and P. Claudy, Polymorphisme de l'hydrure de magnesium sous haute pression, *Mater. Res. Bull.*, 1980, **15**, 1215–1224.
62 H. S. AlMatouk, V. Chihaia and V. Alexiev, Density functional study of the thermodynamic properties and phase diagram of the magnesium hydride, *CALPHAD: Comput. Coupling Phase Diagrams Thermochem.*, 2018, **60**, 7–15.
63 M. Bortz, B. Bertheville, G. Bötter and K. Yvon, Structure of the high pressure phase γ-MgH2 by neutron powder diffraction, *J. Alloys Compd.*, 1999, **287**, L4.
64 H. J. Monkhorst and J. D. Pack, Special points for Brillouin-zone integrations, *Phys. Rev. B*, 1976, **13**, 5188–5192.
65 W.-Y. Chen, J.-J. Tang, Z.-W. Lu, M.-X. Huang, L. Liu, C.-C. He and Y.-J. Zhao, Theoretical investigation of the surface orientation impact on the hydrogen vacancy formation of MgH2, *Surf. Sci.*, 2021, **710**, 121850.
66 M. Yu and D. R. Trinkle, Accurate and efficient algorithm for Bader charge integration, *J. Chem. Phys.*, 2011, **134**, 064111.
67 W. Tang, E. Sanville and G. Henkelman, A grid-based Bader analysis algorithm without lattice bias, *J. Phys.: Condens. Matter*, 2009, **21**, 084204.
68 E. Sanville, S. D. Kenny, R. Smith and G. Henkelman, Improved grid-based algorithm for Bader charge allocation, *J. Comput. Chem.*, 2007, **28**, 899–908.
69 G. Henkelman, A. Arnaldsson and H. Jónsson, A fast robust algorithm for Bader decomposition of charge density, *Comput. Mater. Sci.*, 2006, **36**, 354–360.